Title

Allysine-Targeted Molecular MRI Enables Early Prediction of Chemotherapy Response in Pancreatic Cancer.

Journal

The Journal of cancer research, 84(15)

Authors

Ma, Hua

Esfahani, Shadi

Krishna, Shriya

et al.

Publication Date

2024-08-01

DOI

10.1158/0008-5472.CAN-23-3548

Peer reviewed

HHS Public Access

Author manuscript

Cancer Res. Author manuscript; available in PMC 2025 February 01.

Published in final edited form as:

Cancer Res. 2024 August 01; 84(15): 2549–2560. doi:10.1158/0008-5472.CAN-23-3548.

Allysine-Targeted Molecular MRI Enables Early Prediction of Chemotherapy Response in Pancreatic Cancer

Hua Ma[†,1,2,3], **Shadi A. Esfahani**[†,2,3,4], **Shriya Krishna**[2], **Bahar Ataeinia**[2,3,4], **Iris Y. Zhou**[1,2,3], **Nicholas J. Rotile**[1,2], **Jonah Weigand-Whittier**[2], **Avery T. Boice**[1,2], **Andrew S. Liss**[5], **Kenneth K. Tanabe**[6], **Peter Caravan**[1,2,3,*]

[1]Institute for Innovation in Imaging (i[3]), Department of Radiology, Massachusetts General Hospital, Charlestown, MA, 02129, USA

[2]Athinoula A. Martinos Center for Biomedical Imaging, Department of Radiology, Massachusetts General Hospital, Charlestown, MA, 02129, USA

[3]Department of Radiology, Harvard Medical School, Boston, Massachusetts 02129, United States

[4]Division of Nuclear Medicine and Molecular Imaging, Department of Radiology, Massachusetts General Hospital, Boston, Massachusetts 02114, United States

[5]Department of Surgery, Massachusetts General Hospital, Boston, Massachusetts, Massachusetts, 02114, United States

[6]Division of Gastrointestinal and Oncologic Surgery, Massachusetts General Hospital, Harvard Medical School, Boston, Massachusetts 02114, United States

Abstract

Neoadjuvant therapy (NAT) is routinely used in pancreatic ductal adenocarcinoma (PDAC), but not all tumors respond to this treatment. Current clinical imaging techniques are not able to precisely evaluate and predict the response to neoadjuvant therapies over several weeks. A strong fibrotic reaction is a hallmark of a positive response, and during fibrogenesis allysine residues are formed on collagen proteins by the action of lysyl oxidases (LOX). Here we report the application of an allysine-targeted molecular magnetic resonance imaging (MRI) probe, MnL3, to provide an early, noninvasive assessment of treatment response in PDAC. Allysine increased 2- to 3-fold after one dose of NAT with FOLFIRINOX in sensitive human PDAC xenografts in mice. Molecular MRI with MnL3 could specifically detect and quantify fibrogenesis in PDAC xenografts. Comparing the MnL3 signal before and 3 days after one dose of FOLFIRINOX predicted subsequent treatment response. The MnL3 tumor signal increased by 70% from day 0 to day 3 in mice that responded to subsequent doses of FOLFIRINOX, while no signal increase was

[*]**Corresponding author:** Peter Caravan, Ph.D. Athinoula A. Martinos Center for Biomedical Imaging, Institute for Innovation in Imaging (i[3]), Department of Radiology, Massachusetts General Hospital, Harvard Medical School, 149 Thirteenth St, Suite 2301, Charlestown, MA 02129, United States. pcaravan@mgh.harvard.edu.
[†]Equal contribution

Conflicts of Interest:
H.M. and P.C. are inventors of a filed patent based on the work here (Molecular probes for in vivo detection of aldehydes, PCT/WO2022241470). P.C. has equity in and is a consultant to Collagen Medical LLC, has equity in Reveal Pharmaceuticals Inc., and has research support from Transcode Therapeutics. The other authors declare that they have no competing interests.

observed in FOLFIRINOX-resistant tumors. This study indicates the promise of allysine-targeted molecular MRI as a noninvasive tool to predict chemotherapy outcomes.

Introduction:

Pancreatic ductal adenocarcinoma (PDAC) is a significant public health issue globally and is predicted to be the second most deadly cancer in the United States by 2030 (1). Although the treatment of PDAC has improved over recent years, the prognosis is still dismal, with a five-year overall survival of only 11% (2). Unfortunately, only approximately 15 – 20% of the patients are diagnosed at an early stage and considered as candidates for upfront surgical resection. Due to the late onset of symptoms and the aggressiveness of the disease, most patients are diagnosed at locally advanced or metastatic stages. The combination of oxaliplatin, irinotecan, folinic acid and 5-flourouracil in a regimen called FOLFIRINOX is effective against PDAC. Neoadjuvant therapy (NAT) with FOLFIRINOX, particularly in patients with locally advanced tumors, with or without chemoradiotherapy, has become the first-line standard of care for this disease (3–5).

Unfortunately, not all patients with PDAC have tumors that respond to FOLFIRINOX NAT, with a reported response rate of 31.6% (6). Moreover, conventional radiographic assessment do not accurately capture responsiveness to FOLFIRINOX NAT (7). Better diagnostic tools are needed to both characterize and predict response to FOLFIRINOX NAT.

Response of PDAC to neoadjuvant therapy is an important predictor of survival (8,9). Currently, histologic evaluation of tumors by pathologists for grading of the extent of tumor regression remains the diagnostic gold standard for the histological assessment of the effect of NAT in patients (10,11). However biopsies are not obtained after NAT to determine responsiveness, and NAT response is only assessed histologically after resection. In recent years, however, there has been growing concern about the inherent flaws of tumor regression grading systems and their imprecise and impractical criteria that result in divergence of practice and lack of interobserver agreement (12). The invasive nature of this procedure exposes patients with a high risk of major complications such as infection and is not suitable for longitudinal monitoring of treatment response. In addition, tumor sampling does not capture the state of response across metastatic sites. With advances in imaging technology, data acquisition, and analysis, more studies are being conducted to improve imaging accuracy for noninvasive evaluation of the response to NAT for PDAC. In the clinic, high-resolution CT and MRI at approximately 2-month intervals are standard-of-care imaging modalities for monitoring the response of PDAC to NAT. However, studies have shown that all these methods suffer from shared drawbacks in that there were few morphological changes in the tumors, and only a small percentage of patients showed tumor shrinkage during the long course of standard cytotoxic NAT (13,14). While ^{18}F-FDG PET has been widely used to evaluate response to various forms of therapy in many cancer types (15–17), its use in the setting of PDAC has been limited by multiple factors (18). These limitations include the occurrence of nonspecific uptake of ^{18}F-FDG in inflammatory lesions and regions of infection, and an inability to reliably distinguish focal mass-forming pancreatitis from pancreatic cancer.

It was shown that, in patients, PDAC fibrosis observed on post-chemoradiation biopsies was associated with extended overall survival (19–21). Erstad et al. showed that in different orthoptic PDAC mouse models, collagen deposition after FOLFIRINOX treatment could be detected with type I collagen-targeted molecular MRI (20). However, collagen deposition is complex and requires time for collagen levels to build up to levels detectable by molecular MRI. Lysyl oxidase (LOX) and its paralogs are established markers of fibrogenesis (Fig. 1A) (22). During fibrogenesis, the secretion and enzymatic activity of LOX and its paralogs are increased (23). LOX catalyzes the oxidation of lysine residues to lysyl-aldehydes (allysine) that then undergo spontaneous reactions with adjacent lysine, hydroxylysine, or other allysine residues on nearby collagen proteins to form cross-links (24). Although the LOX-mediated oxidation of lysine residues is catalytic, subsequent condensation reactions between proteins are slow, and thus there is a buildup of extracellular allysine during fibrogenesis. Taking advantage of the rapid and reversible hydrazine or oxyamine condensation reaction with aldehydes to form stable hydrazones or oximes, we developed paramagnetic complexes functionalized with hydrazine or oxyamine moieties as molecular MRI probes for noninvasive quantification of fibrogenesis. Using these probes, we previously showed that molecular MRI of extracellular allysine is a sensitive marker of the early onset of fibrosis in the liver, kidney, and lung (25–30). In a model of liver fibrosis, allysine-targeted molecular MRI could detect the early onset of fibrosis before there was a significant buildup of collagen as assessed histologically and biochemically (25,26).

We recently reported MnL3, a macrocyclic manganese (Mn^{2+}) chelate based on [Mn(PC2A)(H_2O)] with a pendant alkyl hydrazine for targeting aldehydes in the extracellular space, and MnL4, which is a structurally similar compound incapable of targeting aldehydes that serves as a negative control (Fig. 1B)(31). Like Gd^{3+} complexes that are used as contrast agents in clinical MRI, complexes based on Mn^{2+} are also potent relaxation agents that shorten T1 and enhance signal in T1-weighted MR protocols. However unlike gadolinium, manganese is an essential element which may confer a safety advantage over gadolinium-based complexes. The T1 relaxivities of MnL3 and MnL4 were similar in PBS (3 $mM^{-1}s^{-1}$) and unchanged in bovine serum albumin (BSA), indicating efficient proton relaxation and no appreciable nonspecific protein binding of the probes. However, the relaxivity of MnL3 exhibited a 4-fold increase when bound to aldehyde-enriched BSA, while no enhancement was observed with MnL4. These results indicate the specificity of MnL3 in targeting aldehyde, and the increase in relaxivity upon binding provides additional signal enhancement in T1-weighted MRI, which should lead to higher sensitivity. MnL3 and MnL4 showed similar pharmacokinetics in mice, with rapid renal elimination and no accumulation in healthy tissue. That study also demonstrated that MnL3-enhanced MRI, but not MnL4, specifically detected pulmonary fibrogenesis in a mouse lung injury model, and MR signal enhancement correlated strongly with lung allysine concentration. This combination of favorable features make MnL3 a strong candidate for clinical translation. Additionally, we recently showed that aldehyde-targeted molecular MR in rodent models of liver fibrosis was extremely sensitive to fibrogenesis and could detect the onset of fibrotic liver disease before liver collagen levels had significantly increased (25,26). Here we hypothesize that aldehyde-targeted molecular MRI with MnL3 can provide an early readout of the FOLFIRINOX chemotherapy treatment response in mouse models of PDAC.

Materials and methods:

Ethics approval of animals and cell lines

All animal experiments were performed in accordance with the National Institutes of Health's *Guide for the Care and Use of Laboratory Animals* and in compliance with the Animal Research: Reporting of In Vivo Experiments (ARRIVE) guidelines and approved by the Massachusetts General Hospital (MGH) Institutional Animal Care and Use Committee (protocol 2019N000139). Animals were housed under controlled temperature and 12-hour light/12-hour dark cycle conditions. In all the experiments, mice were randomized to different groups. Evaluation of the probes in animals was performed in a nonblinded fashion but using the same caliper and same analyst to decrease the variability. Investigators were blinded for histological analyses. The number of biological replicates and statistical results are indicated in the figure legends.

Patient-derived metastatic pancreatic cancer cells, PDAC6, were obtained from the Ting laboratory at MGH (32), metastatic PDAC cells, 1319 were obtained from the Liss laboratory at MGH (33), primary PDAC cells, PANC1, were obtained from ATCC (34). All cells were cultured in RPMI medium (ATCC) supplemented with 10% fetal bovine serum (Thermo-Fisher) and 1% penicillin–streptomycin (ThermoFisher) at 37 °C and 5% CO_2. Approximately 1×10^6 cells in PBS were mixed with Matrigel (BD Biosciences) in a total volume of 100 μL 1:1 (v/v) and injected into the subcutaneous space of the mice over the right lower back. The tumors were monitored daily and once reached approximately 200 mm^3, they were randomized into the experimental groups.

Drug formulation and administration

The chemotherapy regimen, FOLFIRINOX was prepared by dissolving calcium folinate (Sigma-Aldrich, C0250000, 15 mg/mL), oxaliplatin (Sigma-Aldrich, Y0000271, 0.75 mg/mL), irinotecan hydrochloride (Sigma-Aldrich, PHR2717, 7.5 mg/mL), and 5-fluorouracil (Sigma-Aldrich, F6627, 7.5 mg/mL) in sterilized saline. The drug solution was prepared freshly before administration to the mice to prevent degradation. For treatment of the tumor, a solution of the prepared drug was administrated in the mouse tail vein every 3 days, containing 50 mg/kg calcium folinate, 2.5 mg/kg oxaliplatin, 25 mg/kg irinotecan hydrochloride, and 25 mg/kg 5-fluorouracil (total volume < 150 μL) (20). Intravenous sterile saline (i.v. < 150 uL) was used as the vehicle in the control group experiments.

Molecular MRI probes

MnL3 is a Mn(II)-PC2A probe derivatized with an allysine-targeting hydrazine moiety, and MnL4 is a structure-matched non-binding control probe. Both probes have relaxivity of approximately 3.1 mM^{-1} s^{-1} in PBS (1.4 T, 37 °C). MnL3 can covalently bind to a allysine-modified bovine serum albumin (BSA-Ald) and exhibits a relaxivity of 12.7 mM^{-1} s^{-1} after binding, while MnL4 exhibits low/no binding to BSA-Ald. The probes were synthesized using a previously published protocol (31).

Animal experiments

A total of 63 tumor-bearing male nude mice (Crl:NU(NCr)-Foxn1nu, strain 490, Charles River Laboratories, MA, USA) were included in this study.

To evaluate the specificity of the MnL3 probe to target allysine in vivo, a total of 18 PDAC6 tumor-bearing mice were used. Mice were randomized into three major groups (n=4 per group) to undergo MR imaging prior to receiving any treatment (day 0), after one dose of FOLFIRINOX (dosing on day 0, imaging on day 3), or after two doses of FOLFIRINOX (dosing on days 0 and 3, imaging on day 7). In each group, mice underwent MRI prior to and up to 60 min after injection of MnL4 (0.1 mmol/kg, i.v.). The same mice underwent a repeat MRI 4 hours later, using the MnL3 (0.1 mmol/kg, i.v.) probe. Immediately after the second scan (60 min after administration of MnL3), the mice were euthanized, and the tumors were harvested for ex vivo analyses. An additional 2 mice per group were injected with MnL3 probe and euthanized at the same time post-injection for ex vivo analyses (for a total of 6 mice/group). One mouse from the third group died after the second FOLFIRINOX treatment and was excluded from the study.

To evaluate the ability of MnL3 probe to differentiate responders from non-responders, a total of 25 mice with FOLFIRINOX-sensitive PANC1 xenografts and 20 mice with FOLFIRINOX-resistant 1319 xenografts were used. A subgroup of mice underwent a baseline MnL3 enhanced MRI at day 0 (n = 16 for PANC1 and n = 8 for 1319). After imaging, all the mice were randomized into two major groups of treatment with saline as vehicle control or FOLFIRINOX. A repeat MnL3 enhanced MRI was performed 3 days after receiving the first dose of treatment (day 3). For PANC1 tumor-bearing mice, following the second imaging experiment, 6 mice from each group (12 in total) were euthanized, and the tumors were extracted for ex vivo validations. The remaining imaged PANC1 tumor-bearing mice plus 9 additional mice continued to receive treatment with either vehicle or FOLFIRINOX every 3 days, and the tumor growth was monitored for a total of 21 days. Two mice from FOLFIRINOX-treated group did not survive until the study endpoint and were excluded from the study. For 1319 tumor-bearing mice, following the second imaging, the 8 imaged mice were euthanized, and tumors were harvested for ex vivo validations. An additional 2 mice (one from each group) were administrated with MnL3 (0.1 mmol/kg, i.v.), euthanized 60 min after injection, and tumors were harvested for ex vivo validations. The remaining 10 mice continued to receive treatment with either FOLFIRINOX or vehicle every 3 days and the tumor growth was monitored for a total of 21 days. Two mice from FOLFIRINOX-treated group did not survive until the study endpoint and were excluded from the study.

MRI imaging and analysis

Animals were imaged on a 4.7 T MRI scanner (Bruker Biospec) using a 35 mm i.d. transmit/receive linear bird-cage coil (Bruker, BIO PRK 200 MIM 35/59). During MR imaging, animals were anesthetized with 1–2% isoflurane and air/oxygen mixture to maintain a constant respiration rate (60 ± 10 breaths per min), kept warm by a thermal pad, and monitored by a small animal physiological monitoring system (SA Instruments Inc., Stony

Brook NY). The tail vein was cannulated for delivery of the molecular probe (0.1 mmol/kg, 30 mM stock solution as determined by ICP-MS).

MR imaging sequences: 3D T1 FLASH (TR/TE/FA = 16 ms/2 ms/30°, 0.4 mm isotropic spatial resolution, field of view (FOV) 60 mm × 35 mm, two averages, acquisition time = 4 min) images were acquired before and dynamically after injection of the probe to quantify the signal enhancement; DCE-MRI (TR/TE/FA = 65 ms/2 ms/30°, resolution 0.4 × 0.5, 2 mm slice thickness, FOV 64 × 51 mm, one average, acquisition time = 6.5 min, temporal resolution 5.6 s) was acquired 1 min prior to and immediately following probe administration for another 5 min. During DCE-MRI, the probe was intravenously administered at an injection rate of 50 μL/s, followed by a 50 μL saline flush; T2 RARE (TR/TE/FA = 2000 ms/27 ms/180°, resolution 0.2 × 0.2, 1 mm slice thickness, FOV 35 mm × 35 mm, two averages, acquisition time = 3 min) images were acquired before probe injection to define the tumor region of interest (ROI) and to identify areas of tumor necrosis.

MRI Data analysis: Image visualization and quantification were performed in Amide software (AMIDE-bin 1.0.5) (35). Using the T2 RARE image to identify regions of necrosis, a 3D ROI was manually traced on the first post-injection T1 FLASH image encompassing the entire tumor parenchyma while avoiding regions of necrosis. A second 3D ROI was placed on the adjacent phantom to quantify the signal intensity of the phantom for normalization. These ROIs were copied to the pre- and post-injection FLASH images. The normalized signal intensity (nSI) was computed by normalizing the signal intensity of the tumor (SI_t) to the signal intensity of the phantom (SI_p), and the increase in nSI relative to the image acquired before probe injection was computed (%nSI). For the DCE image, an ROI was placed in the tumor parenchyma. A second ROI was placed on the adjacent phantom to compute the normalized signal intensity and copied to all the DCE images to creating a time-intensity curve. The peak %nSI was computed from these curves.

Tissue analysis for mice

After imaging, the animals were euthanized, and the tumors were harvested. A piece of each tumor was embedded in paraffin and then sectioned into 5-μm-thick slices for later staining with MT, H&E, and LOX. Another piece of each tumor was snap-frozen in liquid nitrogen for quantitative analyses of allysine and manganese content.

Masson's Trichrome staining and hematoxylin and eosin staining of the slices were performed by the MGH Pathology Core. For LOX IHC performed on paraffin-embedded section, after deparaffinization and dehydration, slides were blocked with PBST (2% Triton in PBS) for 15 min followed by incubation with rabbit monoclonal to LOX antibody (Abcam, ab174316, 1:1000 dilution with 5% goat serum) for 60 min at room temperature. After that, the slides were incubated with 3% H_2O_2 at room temperature to block endogenous peroxidase activity. The slides were then incubated with biotinylated secondary antibody (Merck, Goat Anti-Rabbit and Anti-Mouse, 3523293) for 60 min, followed by washing with PBST and then 10 min incubation with Streptavidin HRP Conjugate (Merck, OR03L, 1:400). After washing with PBST, the slides were incubated with metal enhanced DAB (Thermo, 1:10) and then nuclei were counterstained with hematoxylin (1:6) for 30 s.

The whole slides were fully digitalized using a NanoZoomer 2.0-HT whole-slide scanner (Hamamatsu Photonics). The CPA, defined as the percentage of the area of the stained positive by MT, and the LOX positive area, defined as the percentage of the area of the stained positive by DAB, were measured with ImageJ (Fiji, version 1.0). Allysine and manganese content in the tumor were quantified using reported HPLC and ICP-MS methods, respectively and expressed as the amount per wet weight of tissue (nmol/g) (31).

Statistical analysis

Data are shown as box plots with central marks indicating the median, bottom and top edges of the box indicating the interquartile range, and top and bottom marks indicating the maximum and minimum data points. Bar graphs are shown as mean ± standard deviation (SD). Tumor volume measurements were shown as mean ± standard error of mean (SEM). Statistical analysis was performed using GraphPad Prism (version 9.1.1). Comparisons were performed with two-tailed unpaired Student's t-test to analyze differences between two different groups, paired Student's t-test to analyze differences in variables for the same mice in two different time points, or one-way ANOVA with Tukey's post hoc comparison to analyze differences among three or more groups. Values of $P < 0.05$ were considered statistically significant. Sample sizes can be found in the figure legends and were chosen based on previous experience. Animals were fully randomized.

Data availability

The data generated in this study are available within the article and Supplementary data files and upon request from the corresponding author.

Results:

MnL3 is an aldehyde-reactive MRI probe with greater reactivity under acidic conditions.

We previously showed that MnL3, but not MnL4, reacts very rapidly with aldehydes (31). Since the extracellular tumor microenvironment is often acidic, we first tested how the rate of aldehyde condensation was affected by pH. The reactivity of MnL3 and MnL4 to allysine was conducted using butyraldehyde as a small-molecule model for allysine. After incubation of MnL3 or MnL4 with butyraldehyde, aliquots of the solution were analyzed by HPLC-MS with UV and mass spectrometry detection at different incubation times. Fig. 1C and Fig. S1 show that MnL3 reacts completely with butyraldehyde at both pH 6.5 and pH 7.4. Fig. 1D and Fig. S2 show that MnL4 does not react with butyraldehyde. Measuring the condensation rate as a function of time indicated that MnL3 reacts twice as fast with butyraldehyde at pH 6.5 ($10.4 \pm 1.4\ M^{-1}s^{-1}$) compared to pH 7.4 ($4.6 \pm 0.3\ M^{-1}s^{-1}$), suggesting that MnL3 will have a faster on-rate in the acidic tumor microenvironment, Fig. 1E.

MnL3 MR imaging specifically targets and quantifies allysine within the PDAC stroma in animal models of PDAC.

First, the fibrotic response of PDAC tumor stroma to FOLFIRINOX was validated histologically and biochemically in a patient-derived PDAC6 xenograft model. Fig. 2A shows representative H&E stained tissue for untreated tumor and for tumors harvested 3 days after one or two doses of FOLFIRINOX. Biochemically quantified allysine in the

extracted tumor tissues showed a significantly higher allysine content as early as 3 days post-treatment (95 ± 15 nmol/g, P = 0.007, n = 6), which remained significantly elevated at 7 days post-treatment (108 ± 32 nmol/g, P = 0.001, n= 5) compared to untreated tumors (55 ± 15 nmol/g, n = 6, Fig. 2B). Collagen staining with Masson's Trichrome (MT) showed no significant change in the collagen proportion area (CPA) 3 days after one dose of FOLFIRINOX (20 ± 8 %, P > 0.5, n = 5) but was significantly increased after two doses of FOLFIRINOX treatment (28 ± 8 %, P = 0.01, n = 5) compared to the untreated tumors (12 ± 4 %, n = 5, Fig. 2C, and D). On the other hand, immunohistochemical (IHC) staining of tumor tissues slides revealed a significantly elevated LOX staining compared to the untreated tumors after one FOLFIRINOX dose (%LOX positive area: 28 ± 6 %, P = 0.01, n = 6) which further increased after two doses of treatment (%LOX positive area: 39 ± 7 %, P < 0.001, n= 5) compared to the untreated tumors (%LOX positive area: 15 ± 7 %, n = 5, Fig. 2E and F).

The specificity of MnL3 molecular MR to tumor stromal allysine was evaluated in the PDAC6 xenograft model (Fig. 3A). In untreated mice, dynamic MnL4 enhanced T1w FLASH MRI showed tumor signal enhancement that peaked by 7 min post-injection (p.i.) (Fig. S3) and then washed out with the tumor signal returning to its pre-injection baseline value by 60 min p.i. (Fig. 3B and C). On the other hand, MnL3 enhanced MR performed in the same mice resulted in higher initial tumor signal enhancement compared to MnL4, and the tumor signal enhancement persisted over 60 min p.i. (Fig. 3B and C). The %nSI of the tumors by MnL3 was significantly higher than MnL4 at 30 min and 60 min p.i. (at 60 min p.i., %nSI: 14.9 ± 2.7 % vs. 0.4 ± 3.8 %, MnL3 vs. MnL4, P = 0.003, n = 4, Fig. 3C and 30 min p.i. data shown in Fig. S4).

In the next step, the specificity of the MnL3 probe to allysine changes in response to chemotherapy was evaluated after one dose (dosed at day 0, imaged at day 3, n=4) and after 2 doses (dosed at days 0 and 3, imaged at day 7, n=4) of FOLFIRINOX treatment. There was an increase in tumor signal enhancement by the MnL3 probe after one or two doses of FOLFIRINOX compared with the pre-treatment baseline value (at 60 min p.i., 14.9 ± 2.7 % at day 0, 25.3 ± 5.2 % at day 3, and 29.3 ± 7.2% at day 7; day 3 vs day 0: P = 0.04, day 7 vs day 0: P = 0.003, n = 4 for each group, Fig 3C). On the other hand, MnL4 enhanced MR showed no difference in transient tumor signal enhancement among the three imaging time points for the same tumor-bearing mice (at 60 min p.i., day 3 vs day 0: P > 0.99, day 7 vs day 0: P > 0.99, n = 4 for each group, Fig 3C).

Dynamic contrast-enhanced (DCE)-MRI within the initial 5 min p.i. of MnL4 showed no significant differences between upslope of tumor signal enhancement, the peak tumor %nSI, or the washout rate before or after FOLFIRINOX (Fig. 3D and Fig. S5). Fig. 3D shows peak %nSI and the entire DCE %nSI versus time curves for MnL4 are shown in Fig. S5 and are superimposable indicating that no large change in tumor permeability and/or extracellular volume is occurring in response to treatment. Ex vivo quantification of tumor manganese content at 60 min p.i. of MnL3 (Fig. S6) was consistent with the MRI results and was higher at 3 days (41 ± 6 nmol/g, P = 0.05, n= 6) and 7 days (42 ± 9 nmol/g, P = 0.04, n= 5) after FOLFIRINOX treatment compared to the untreated tumors (29 ± 8 nmol/g, n= 6). The

tumor %nSI at 60 min p.i. of MnL3 correlated well with biochemically quantified allysine concentration (Fig. 3E).

MnL3 molecular MR imaging can predict response to FOLFIRINOX treatment in mouse models of PDAC.

We next examined whether MnL3 MRI can predict PDAC response to FOLFIRINOX chemotherapy. Specifically, we tested whether the MnL3 tumor signal enhancement measured at 3 days after the first FOLFIRINOX treatment relative to the pre-treatment scan can predict response. For this purpose, two subcutaneously implanted PDAC models using patient-derived FOLFIRINOX-sensitive PANC1 cells (n = 23) and FOLFIRINOX-resistant 1319 cells (n = 18) were employed.

Fig. 4A shows representative H&E stained tissue for untreated PANC1 tumor and for tumors harvested 3 days after one dose of FOLFIRINOX. For the FOLFIRINOX-sensitive PANC1 tumor-bearing mice, biochemical assessment of tumor allysine concentration by HPLC showed a significant increase after FOLFIRINOX treatment compared to vehicle (97 ± 33 nmol/g vs. 35 ± 15 nmol/g, FOLFIRINOX group vs. vehicle group, P = 0.01, n = 4 for each group, Fig. 4B). Histological staining of the extracted PANC1 tumors exhibited significantly higher CPA on MT staining in tumors treated with one dose of FOLFIRINOX compared to vehicle (CPA: 23 ± 14 % vs. 8 ± 5 %, FOLFIRINOX group vs. vehicle group, respectively, P = 0.04, n= 6 for each group, Fig. 4C and D), and significantly higher LOX staining on IHC (%LOX positive area: 24 ± 11 % vs. 8 ± 5 %, FOLFIRINOX group vs. vehicle group, respectively, p = 0.009, n = 6 for each group, Fig. 4E and F).

Quantification of MnL3 enhanced MRI in the FOLFIRINOX-sensitive PANC1 tumor-bearing mice at day 0 (before treatment) showed that mice assigned to both the FOLFIRINOX and vehicle groups exhibited equivalent tumor signal enhancement (13.2 ±2.7 % vs. 12.8 ± 2.7 %, FOLFIRINOX group vs. vehicle group, P = 0.7, n = 8 for each group, Fig. S7). In vehicle-treated mice, there was no change in the tumor signal enhancement at 3 days post-treatment compared to the pre-treatment scan (12.8 ± 2.7% vs. 12.9 ± 2.9 %, pre-treatment vs. post-treatment, P = 0.9, n = 8 for each group, Fig. 5A, B and C). While in the FOLFIRINOX-treated group, the tumor MnL3 MR signal enhancement was significantly increased by 70 % at day 3 relative to day 0 (13.3 ± 2.7 % vs. 22.5 ± 3.2 %, pre-treatment vs. post-treatment, P < 0.001, n = 8 for each group, Fig. 5D). Ex vivo assessment of tumor manganese content by ICP-MS method at 60 min p.i. of MnL3 showed a significantly elevated manganese content in FOLFIRINOX-treated mice compared to the vehicle-treated mice (50 ± 16 nmol/g vs. 25 ± 7 nmol/g, FOLFIRINOX group vs. vehicle group, P = 0.03, n = 4 for each group, Fig. S8). Monitoring the tumor growth every 3 days for a total of 21 days showed effectiveness of FOLFIRINOX in inhibiting tumor growth compared to vehicle-treated group (FOLFIRINOX vs. vehicle, P < 0.001, respectively, Fig. 5E).

Fig. 6A shows representative H&E stained tissue for untreated 1319 tumor and for tumors harvested 3 days after one dose of FOLFIRINOX. For the FOLFIRINOX-resistant 1319 tumor-bearing mice, biochemical assessment of tumor allysine concentration showed no significant difference in the values between FOLFIRINOX- and vehicle-treated mice (94 ±

24 nmol/g vs. 100 ± 37 nmol/g, FOLFIRINOX group vs. vehicle group, P = 0.8, n = 5 for each group, Fig. 6B). Fibrosis quantified by CPA and fibrogenesis assessed by LOX IHC in the extracted 1319 tumor tissues showed that one dose of FOLFIRINOX did not induce a significant change in either tumor collagen deposition or LOX expression (CPA(%): 24 ±4 % vs. 18 ± 5 %, FOLFIRINOX vs. vehicle, P = 0.08, n = 5 for each group, Fig. 6C and D; LOX positive area(%): 34 ± 7 % vs. 29 ± 6 %, FOLFIRINOX vs. vehicle, P = 0.2, n = 5 for each group, respectively, Fig. 6E and F).

In the FOLFIRINOX-resistant 1319 tumor-bearing mice, both groups of FOLFIRINOX and vehicle-treated mice exhibited similar tumor signal enhancement on MnL3 MRI at day 0 (18.2 ± 4.7 vs. 17.2 ± 5.1, FOLFIRNOX group vs. vehicle group, P = 0.8, n = 4 for each group, Fig. S9,), and the signal did not significantly increase after 3 days (one dose) of either FOLFIRINOX or vehicle (P = 0.7 for vehicle group and P = 0.6 for FOLFIRINOX group, Fig. 7A – D,). Ex vivo determination of tumor manganese concentration at 60 min p.i. of MnL3 (37 ± 10 nmol/g vs. 42 ± 16 nmol/g, FOLFIRINOX group vs. vehicle group, n = 5 for each group, Fig. S10) showed no significant difference in the values between FOLFIRINOX- and vehicle-treated mice, in line with the findings from in vivo MRI. Monitoring the animals over 21 days revealed that FOLFIRNOX-treated mice showed no treatment benefit compared to the vehicle-treated mice with respect to tumor volume change (FOLFIRINOX vs. vehicle, P = 0.8, Fig. 7E).

Discussion:

PDAC remains one of the most significant challenges in oncology. Surgical resection is the only curative option, available to only 15% of the patients, with long-term survival after R0 resection approaching 25% (36). Despite considerable progress in advanced surgical techniques and neoadjuvant chemotherapy that has resulted in downstaging and increasing the chance of resectability in patients with local disease, long-term survival (≥ 5 years) remains low for most patients.

A significant barrier to assessing NAT effectiveness is the lack of radiological modalities to accurately assess response (37). Clinical restaging during and after NAT is based on MRI or CT metrics, most importantly, the change in lesion size. However, these scan metrics are not predictive of resectability or pathological response in PDAC (38,39). Therefore, noninvasive prediction of PDAC tumor response to NAT is a critical unmet clinical need for this large, difficult-to-treat patient population. FOLFIRINOX is associated with moderate toxicity (40). Early prediction of treatment response would allow futile therapy to be discontinued and avoid unnecessary toxicity. Early determination of resistance to therapy also allows for alternative treatments to start sooner.

We hypothesized here that the fibrotic response that accompanies a successful FOLFIRINOX treatment could be detected noninvasively by molecular MR imaging using the allysine-targeted MRI probe MnL3. Since the tumor microenvironment in PDAC has lower pH values (41), we first demonstrated that MnL3 could still react with aldehydes at the lower pH values and found that MnL3 reacts twice as fast at pH 6.5 compared to pH 7.4. We next tested the specificity of MnL3-enhanced MR for tumor-associated

fibrogenesis in a PDAC xenograft model. While MnL3 and its non-binding control probe MnL4 both provided tumor signal enhancement immediately after i.v. administration owing to non-specific distribution, the tumor signal enhancement with MnL3 persists while the MnL4 enhanced tumor signal washed out with time. The delayed phase tumor signal enhancement with MnL3 correlated linearly with tumor allysine levels. We next showed that one dose of FOLFIRINOX chemotherapy resulted in elevated tumor fibrogenesis, and this could be robustly detected by MnL3-enhanced MRI. To validate the feasibility of MnL3 molecular MRI to predict treatment response, another two patient-derived PDAC xenograft mouse models were prepared using FOLFIRINOX-sensitive and -resistant cell lines. In the FOLFIRINOX-sensitive PDAC xenograft, one dose of FOLFIRINOX treatment resulted in a 70% increase in MnL3 tumor signal enhancement, and this signal increase predicted the subsequent successful response to treatment. In the FOLFIRINOX-resistant PDAC xenograft, there was no additional MnL3 tumor signal enhancement following one dose of FOLFIRINOX treatment, and this lack of imaging response also predicted the lack of treatment response in this model.

Identifying an effective measure of PDAC treatment response is an active research area. ^{18}F-FDG PET has been studied in the context of NAT for PDAC (18). While ^{18}F-FDG PET combined with contrast-enhanced CT or MRI has been shown to improve the prediction of pathologic response and survival compared to current imaging, the increase in diagnostic accuracy is modest (42–45). Tumor uptake of ^{18}F-FDG could be impacted by the blood glucose level, particularly in PDAC patients, many of whom suffer from diabetes mellitus (43). In addition, lower uptake of ^{18}F-FDG may occur in other pancreatic lesions such as intraductal papillary mucinous neoplasms, necrotic tumors, liver and peritoneal metastases, and small-sized lesions (46,47). Fibroblast activation protein (FAP)-targeted PET probes have shown promising data in detecting pancreatic cancer (48–50), and trials are underway to assess NAT response (e.g. NCT05262855). Others have targeted phosphorylated histone γH2AX, which forms foci around double-strand DNA breaks in response to effective chemo- or radiotherapy. Antibody-based SPECT and PET probes have been described for monitoring treatment response in different models, including PDAC (43,51–53). However, the antibody-based vector requires a long period (e.g. 24 h) for probe uptake and background clearance.

Compared to these nuclear imaging methods, MnL3-enhanced MR may offer several advantages. Rather than adding another imaging test, the MnL3 acquisition could be added to an existing MRI in a multiparametric protocol that could include diffusion, dynamic contrast-enhanced imaging, and tumor morphometry. There is no radiation involved with MnL3, and the spatial resolution of MRI is far superior to that of PET or SPECT (54). MnL3 is readily prepared on a large scale, is shelf stable and can be used at any time and does not require a complex manufacturing and distribution system like radiopharmaceuticals. MnL3 uses the essential element manganese for signal generation instead of the currently used gadolinium-based MRI contrast agents and was shown to undergo rapid renal elimination resulting in near complete elimination within 24 h of administration (31). Unlike ^{18}F-FDG which can be confounded by inflammation, allysine-targeted molecular MR was previously demonstrated to be specific for fibrogenesis and independent of inflammation (55).

Targeting allysine as a biomarker of effective chemotherapy has apparent advantages. Measuring tumor fibrogenesis through allysine expression enables assessment of early response to treatment prior to the change in tumor size. Here we showed that MnL3 enhanced MR could predict treatment response as early as 3 days after the onset of chemotherapy. A fibrotic stroma is a hallmark of PDAC, and while MnL3 showed exquisite sensitivity for measuring increases in fibrogenesis with treatment, we note that in all three animal models, we observed persistent tumor signal enhancement with MnL3. Thus, MnL3-enhanced MRI may also prove useful for the detection and staging of PDAC or more accurate determination of tumor borders and regions of local invasion (56).

However, there are some limitations of the study. First, because of the long Investigational New Drug application process, we could not test this molecular imaging probe in patients. Second, the mouse models of PDAC cancer in this work were xenographically implanted to easily monitor tumor size response to chemotherapy. Finally, the animal models were only treated with FOLFIRINOX in our study. Monitoring treatment response to other chemotherapy regimens with or without radiotherapy is necessary for future clinical translation.

In conclusion, allysine molecular MR with MnL3 provided superior and specific pancreatic tumor signal enhancement compared with non-targeted control probe. MnL3 molecular MR can detect changes in tumor fibrogenesis 3 days after initiation of FOLFIRINOX, and changes in tumor MR signal enhancement predict treatment response. Based on these initial findings in mice, allysine molecular MRI should be explored further for clinical applications in PDAC, including diagnosis , prognostication, and prediction.

Supplementary Material

Refer to Web version on PubMed Central for supplementary material.

Acknowledgments:

This work was supported by grants from the National Cancer Institute: R01CA272876 (ASL), K08CA259626 (SAE), and R25CA174650 (support to SK); the National Institute for Diabetes Digestive and Kidney diseases, R01DK121789 (PC); the National Institutes of Health Office of the Director, S10OD023503 (PC), S10OD025234 (PC), and S10OD032138 (PC); and a Ralph Schlaeger Fellowship Grant from MGH (SAE). We thank Dr. David T. Ting for providing the PDAC6 cell line and Dr. Ting, Dr. Carlos Fernandez de-Castillo and Dr. Pedram Heidari for comments on the manuscript.

Reference:

1. Rahib L, Wehner MR, Matrisian LM, Nead KT. Estimated projection of US cancer incidence and death to 2040. JAMA Netw Open 2021;4:e214708-e
2. Siegel RL, Miller KD, Fuchs HE, Jemal A. Cancer statistics, 2021. Ca Cancer J Clin 2021;71:7–33 [PubMed: 33433946]
3. Gemenetzis G, Groot VP, Blair AB, Laheru DA, Zheng L, Narang AK, et al. Survival in locally advanced pancreatic cancer after neoadjuvant therapy and surgical resection. Ann Surg 2019;270:340–7 [PubMed: 29596120]
4. Rombouts SJ, Walma MS, Vogel JA, van Rijssen LB, Wilmink JW, Mohammad NH, et al. Systematic review of resection rates and clinical outcomes after FOLFIRINOX-based treatment

in patients with locally advanced pancreatic cancer. Ann Surg Oncol 2016;23:4352–60 [PubMed: 27370653]

5. Hackert T, Sachsenmaier M, Hinz U, Schneider L, Michalski CW, Springfeld C, et al. Locally advanced pancreatic cancer: neoadjuvant therapy with folfirinox results in resectability in 60% of the patients. Ann Surg 2016;264:457–63 [PubMed: 27355262]
6. Springfeld C, Ferrone CR, Katz MH, Philip PA, Hong TS, Hackert T, et al. Neoadjuvant therapy for pancreatic cancer. Nat Rev Clin Oncol 2023:1–20
7. Zhang Y, Huang Z-X, Song B. Role of imaging in evaluating the response after neoadjuvant treatment for pancreatic ductal adenocarcinoma. World Journal of Gastroenterology 2021;27:3037–49 [PubMed: 34168406]
8. Truty MJ, Kendrick ML, Nagorney DM, Smoot RL, Cleary SP, Graham RP, et al. Factors predicting response, perioperative outcomes, and survival following total neoadjuvant therapy for borderline/locally advanced pancreatic cancer. Annals of surgery 2021;273:341–9 [PubMed: 30946090]
9. He J, Blair AB, Groot VP, Javed AA, Burkhart RA, Gemenetzis G, et al. Is a pathological complete response following neoadjuvant chemoradiation associated with prolonged survival in patients with pancreatic cancer? Ann Surg 2018;268:1–8 [PubMed: 29334562]
10. Janssen BV, Tutucu F, van Roessel S, Adsay V, Basturk O, Campbell F, et al. Amsterdam International Consensus Meeting: tumor response scoring in the pathology assessment of resected pancreatic cancer after neoadjuvant therapy. Modern Pathology 2021;34:4–12 [PubMed: 33041332]
11. Nagaria TS, Wang H, Chatterjee D, Wang H. Pathology of treated pancreatic ductal adenocarcinoma and its clinical implications. Archives of pathology & laboratory medicine 2020;144:838–45 [PubMed: 32023088]
12. Haeberle L, Esposito I. Pathology of pancreatic cancer. Transl Gastroenterol Hepatol 2019;4:50–62 [PubMed: 31304427]
13. Katz MH, Fleming JB, Bhosale P, Varadhachary G, Lee JE, Wolff R, et al. Response of borderline resectable pancreatic cancer to neoadjuvant therapy is not reflected by radiographic indicators. Cancer 2012;118:5749–56 [PubMed: 22605518]
14. Barreto SG, Loveday B, Windsor JA, Pandanaboyana S. Detecting tumour response and predicting resectability after neoadjuvant therapy for borderline resectable and locally advanced pancreatic cancer. ANZ J Surg 2019;89:481–7 [PubMed: 30117669]
15. Ye Z, Zhu J, Tian M, Zhang H, Zhan H, Zhao C, et al. Response of osteogenic sarcoma to neoadjuvant therapy: evaluated by 18F-FDG-PET. Ann Nucl Med 2008;22:475–80 [PubMed: 18670853]
16. Bastiaannet E, Groen H, Jager P, Cobben D, Van Der Graaf W, Vaalburg W, et al. The value of FDG-PET in the detection, grading and response to therapy of soft tissue and bone sarcomas; a systematic review and meta-analysis. Cancer Treat Rev 2004;30:83–101 [PubMed: 14766127]
17. Westerterp M, van Westreenen HL, Reitsma JB, Hoekstra OS, Stoker J, Fockens P, et al. Esophageal cancer: CT, endoscopic US, and FDG PET for assessment of response to neoadjuvant therapy - Systematic review. Radiology 2005;236:841–51 [PubMed: 16118165]
18. Yeh R, Dercle L, Garg I, Wang ZJ, Hough DM, Goenka AH. The role of 18F-FDG PET/CT and PET/MRI in pancreatic ductal adenocarcinoma. Abdominal Radiology 2018;43:415–34 [PubMed: 29143875]
19. Barenboim A, Lahat G, Geva R, Nachmany I, Nakache R, Goykhman Y, et al. Neoadjuvant FOLFIRINOX for locally advanced and borderline resectable pancreatic cancer: an intention to treat analysis. Eur J Surg Oncol 2018;44:1619–23 [PubMed: 30146251]
20. Erstad DJ, Sojoodi M, Taylor MS, Jordan VC, Farrar CT, Axtell AL, et al. Fibrotic response to neoadjuvant therapy predicts survival in pancreatic cancer and is measurable with collagen-targeted molecular MRI. Clinical Cancer Research 2020;26:5007–18 [PubMed: 32611647]
21. Byrne KT, Betts CB, Mick R, Sivagnanam S, Bajor DL, Laheru DA, et al. Neoadjuvant selicrelumab, an agonist CD40 antibody, induces changes in the tumor microenvironment in patients with resectable pancreatic cancer. Clin Cancer Res 2021;27:4574–86 [PubMed: 34112709]

22. Chen W, Yang A, Jia J, Popov YV, Schuppan D, You H. Lysyl oxidase (LOX) family members: rationale and their potential as therapeutic targets for liver fibrosis. Hepatology 2020;72:729–41 [PubMed: 32176358]
23. Barker HE, Cox TR, Erler JT. The rationale for targeting the LOX family in cancer. Nature Reviews Cancer 2012;12:540–52 [PubMed: 22810810]
24. Rodriguez-Pascual F, Rosell-Garcia T. The challenge of determining lysyl oxidase activity: old methods and novel approaches. Analytical Biochemistry 2022;639:114508–13 [PubMed: 34871563]
25. Ning Y, Zhou IY, Roberts JD Jr, Rotile NJ, Akam E, Barrett SC, et al. Molecular MRI quantification of extracellular aldehyde pairs for early detection of liver fibrogenesis and response to treatment. Science Translational Medicine 2022;14:eabq6297
26. Ning Y, Zhou IY, Rotile NJ, Pantazopoulos P, Wang H, Barrett SC, et al. Dual Hydrazine-Equipped Turn-On Manganese-Based Probes for Magnetic Resonance Imaging of Liver Fibrogenesis. Journal of the American Chemical Society 2022;144:16553–8 [PubMed: 35998740]
27. Chen HH, Waghorn PA, Wei L, Tapias LF, Schühle DT, Rotile NJ, et al. Molecular imaging of oxidized collagen quantifies pulmonary and hepatic fibrogenesis. JCI insight 2017;2:e91506
28. Chen Y-C, Waghorn PA, Rosales IA, Arora G, Erstad DJ, Rotile NJ, et al. Molecular MR Imaging of Renal Fibrogenesis in Mice. Journal of the American Society of Nephrology 2023;34:1159–65 [PubMed: 37094382]
29. Akam EA, Abston E, Rotile NJ, Slattery HR, Zhou IY, Lanuti M, et al. Improving the reactivity of hydrazine-bearing MRI probes for in vivo imaging of lung fibrogenesis. Chemical Science 2020;11:224–31 [PubMed: 32728411]
30. Waghorn PA, Jones CM, Rotile NJ, Koerner SK, Ferreira DS, Chen HH, et al. Molecular Magnetic Resonance Imaging of Lung Fibrogenesis with an Oxyamine-Based Probe. Angew Chem, Int Ed 2017;56:9825–8
31. Ma H, Zhou IY, Chen YI, Rotile NJ, Ay I, Akam EA, et al. Tailored chemical reactivity probes for systemic imaging of aldehydes in fibroproliferative diseases. Journal of the American Chemical Society 2023;145:20825–36 [PubMed: 37589185]
32. Porter RL, Magnus NK, Thapar V, Morris R, Szabolcs A, Neyaz A, et al. Epithelial to mesenchymal plasticity and differential response to therapies in pancreatic ductal adenocarcinoma. Proceedings of the National Academy of Sciences 2019;116:26835–45
33. Huang Y, Nahar S, Nakagawa A, Fernandez-Barrena MG, Mertz JA, Bryant BM, et al. Regulation of GLI underlies a role for BET bromodomains in pancreatic cancer growth and the tumor microenvironment. Clin Cancer Res 2016;22:4259–70 [PubMed: 27169995]
34. Ling Q, Xu X, Wei X, Wang W, Zhou B, Wang B, et al. Oxymatrine induces human pancreatic cancer PANC-1 cells apoptosis via regulating expression of Bcl-2 and IAP families, and releasing of cytochrome c. Journal of Experimental & Clinical Cancer Research 2011;30:1–6
35. Loening AM, Gambhir SS. AMIDE: a free software tool for multimodality medical image analysis. Molecular imaging 2003;2:131–7 [PubMed: 14649056]
36. Stark AP, Sacks GD, Rochefort MM, Donahue TR, Reber HA, Tomlinson JS, et al. Long-term survival in patients with pancreatic ductal adenocarcinoma. Surgery 2016;159:1520–7 [PubMed: 26847803]
37. Perri G, Prakash L, Qiao W, Varadhachary GR, Wolff R, Fogelman D, et al. Response and survival associated with first-line FOLFIRINOX vs gemcitabine and nab-paclitaxel chemotherapy for localized pancreatic ductal adenocarcinoma. JAMA surgery 2020;155:832–9 [PubMed: 32667641]
38. Ferrone CR, Marchegiani G, Hong TS, Ryan DP, Deshpande V, McDonnell EI, et al. Radiological and surgical implications of neoadjuvant treatment with FOLFIRINOX for locally advanced and borderline resectable pancreatic cancer. Ann Surg 2015;261:12–7 [PubMed: 25599322]
39. Wagner M, Antunes C, Pietrasz D, Cassinotto C, Zappa M, Sa Cunha A, et al. CT evaluation after neoadjuvant FOLFIRINOX chemotherapy for borderline and locally advanced pancreatic adenocarcinoma. Eur Radiol 2017;27:3104–16 [PubMed: 27896469]
40. Muranaka T, Kuwatani M, Komatsu Y, Sawada K, Nakatsumi H, Kawamoto Y, et al. Comparison of efficacy and toxicity of FOLFIRINOX and gemcitabine with nab-paclitaxel in unresectable pancreatic cancer. Journal of gastrointestinal oncology 2017;8:566–71 [PubMed: 28736643]

41. Shah VM, Sheppard BC, Sears RC, Alani AW. Hypoxia: Friend or Foe for drug delivery in Pancreatic Cancer. Cancer letters 2020;492:63–70 [PubMed: 32822815]
42. Wilson J, Mukherjee S, Brunner T, Partridge M, Hawkins M. Correlation of 18F-fluorodeoxyglucose positron emission tomography parameters with patterns of disease progression in locally advanced pancreatic cancer after definitive chemoradiotherapy. Clin Oncol 2017;29:370–7
43. Knight JC, Mosley MJ, Bravo LC, Kersemans V, Allen PD, Mukherjee S, et al. 89Zr-anti-γH2AX-TAT but not 18F-FDG allows early monitoring of response to chemotherapy in a mouse model of pancreatic ductal adenocarcinoma. Clinical Cancer Research 2017;23:6498–504 [PubMed: 28774899]
44. Ghaneh P, Wong WL, Titman A, Plumpton C, Vinjamuri S, Johnson C, et al. PET-PANC: Multi-centre prospective diagnostic accuracy and clinical value trial of FDG PET/CT in the diagnosis and management of suspected pancreatic cancer. Journal of Clinical Oncology 2016;34 (15 Suppl):4008 [PubMed: 27646948]
45. Yoo J, Lee JM, Joo I, Lee DH, Yoon JH, Yu MH, et al. Post-neoadjuvant treatment pancreatic cancer resectability and outcome prediction using CT, 18F-FDG PET/MRI and CA 19–9. Cancer Imaging 2023;23:49–62 [PubMed: 37217958]
46. Low G, Panu A, Millo N, Leen E. Multimodality imaging of neoplastic and nonneoplastic solid lesions of the pancreas. Radiographics 2011;31:993–1015 [PubMed: 21768235]
47. Pery C, Meurette G, Ansquer C, Frampas E, Regenet N. Role and limitations of 18F-FDG positron emission tomography (PET) in the management of patients with pancreatic lesions. Gastroenterol Clin Biol 2010;34:465–74 [PubMed: 20688444]
48. Deng M, Chen Y, Cai L. Comparison of 68Ga-FAPI and 18F-FDG PET/CT in the imaging of pancreatic cancer with liver metastases. Clin Nucl Med 2021;46:589–91 [PubMed: 33630809]
49. Chen R, Yang X, Yu X, Zhou X, Ng YL, Zhao H, et al. Tumor-to-blood ratio for assessment of fibroblast activation protein receptor density in pancreatic cancer using [68Ga] Ga-FAPI-04. Eur J Nucl Med Mol Imaging 2023;50:929–36 [PubMed: 36334106]
50. Ding J, Qiu J, Hao Z, Huang H, Liu Q, Liu W, et al. Prognostic value of preoperative [68 Ga] Ga-FAPI-04 PET/CT in patients with resectable pancreatic ductal adenocarcinoma in correlation with immunohistological characteristics. European Journal of Nuclear Medicine and Molecular Imaging 2023;50:1780–91 [PubMed: 36695823]
51. Cornelissen B, Kersemans V, Darbar S, Thompson J, Shah K, Sleeth K, et al. Imaging DNA damage in vivo using γH2AX-targeted immunoconjugates. Cancer Res 2011;71:4539–49 [PubMed: 21586614]
52. Knight JC, Topping C, Mosley M, Kersemans V, Falzone N, Fernández-Varea JM, et al. PET imaging of DNA damage using 89 Zr-labelled anti-γH2AX-TAT immunoconjugates. Eur J Nucl Med Mol Imaging 2015;42:1707–17 [PubMed: 26031435]
53. Cornelissen B, Able S, Kartsonaki C, Kersemans V, Allen PD, Cavallo F, et al. Imaging DNA Damage Allows Detection of Preneoplasia in the BALB-neuT Model of Breast Cancer. J Nucl Med 2014;55:2026–31 [PubMed: 25453049]
54. Rowe SP, Pomper MG. Molecular imaging in oncology: Current impact and future directions. CA: a cancer journal for clinicians 2022;72:333–52 [PubMed: 34902160]
55. dos Santos Ferreira D, Arora G, Gieseck III RL, Rotile NJ, Waghorn PA, Tanabe KK, et al. Molecular MR imaging of liver fibrosis and fibrogenesis is not altered by inflammation. Invest Radiol 2021;56:244–51 [PubMed: 33109919]
56. Polasek M, Yang Y, Schühle DT, Yaseen MA, Kim YR, Sung YS, et al. Molecular MR imaging of fibrosis in a mouse model of pancreatic cancer. Scientific reports 2017;7:8114–24 [PubMed: 28808290]

Statement of Significance:

Allysine-targeted molecular MRI can quantify fibrogenesis in pancreatic tumors and predict response to chemotherapy, which could guide rapid clinical management decisions by differentiating responders from non-responders after treatment initiation.

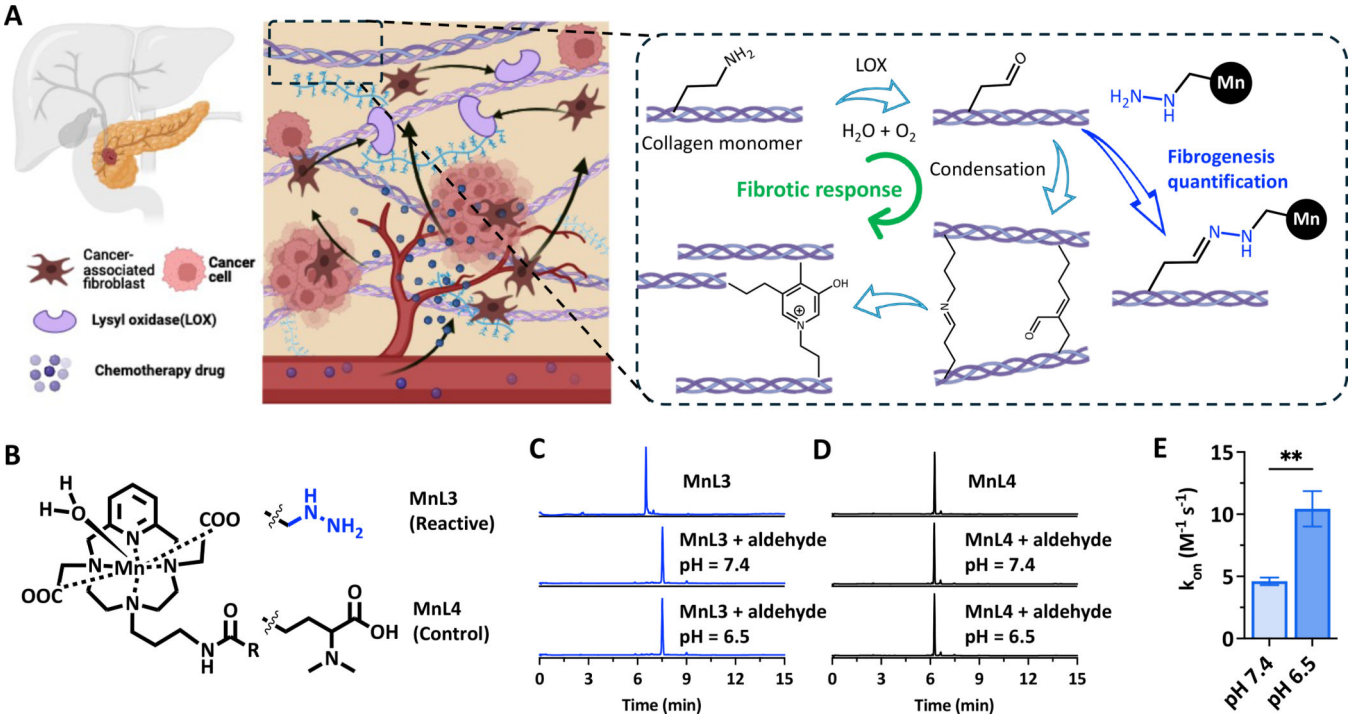

Figure 1.

(**A**) Schematic illustration of the chemotherapy-triggered fibrotic response in tumor and mechanism of allysine-targeted MR probe in detecting tumor fibrogenesis (Created with BioRender.com). (**B**) Structure of hydrazine-bearing allysine-targeted probe MnL3 and non-reactive probe MnL4. MnL3 (**C**) can rapidly react with small molecule aldehyde (butyraldehyde) at either pH 7.4 or pH 6.5, while MnL4 (**D**) does not. (**E**) MnL3 reacts twice as fast with butyraldehyde at pH 6.5 (10.4 ± 1.4 $M^{-1}s^{-1}$) compared to pH 7.4 (4.6 ± 0.3 $M^{-1}s^{-1}$) (n = 3 , Student's t-test, two-tailed, **P < 0.01).

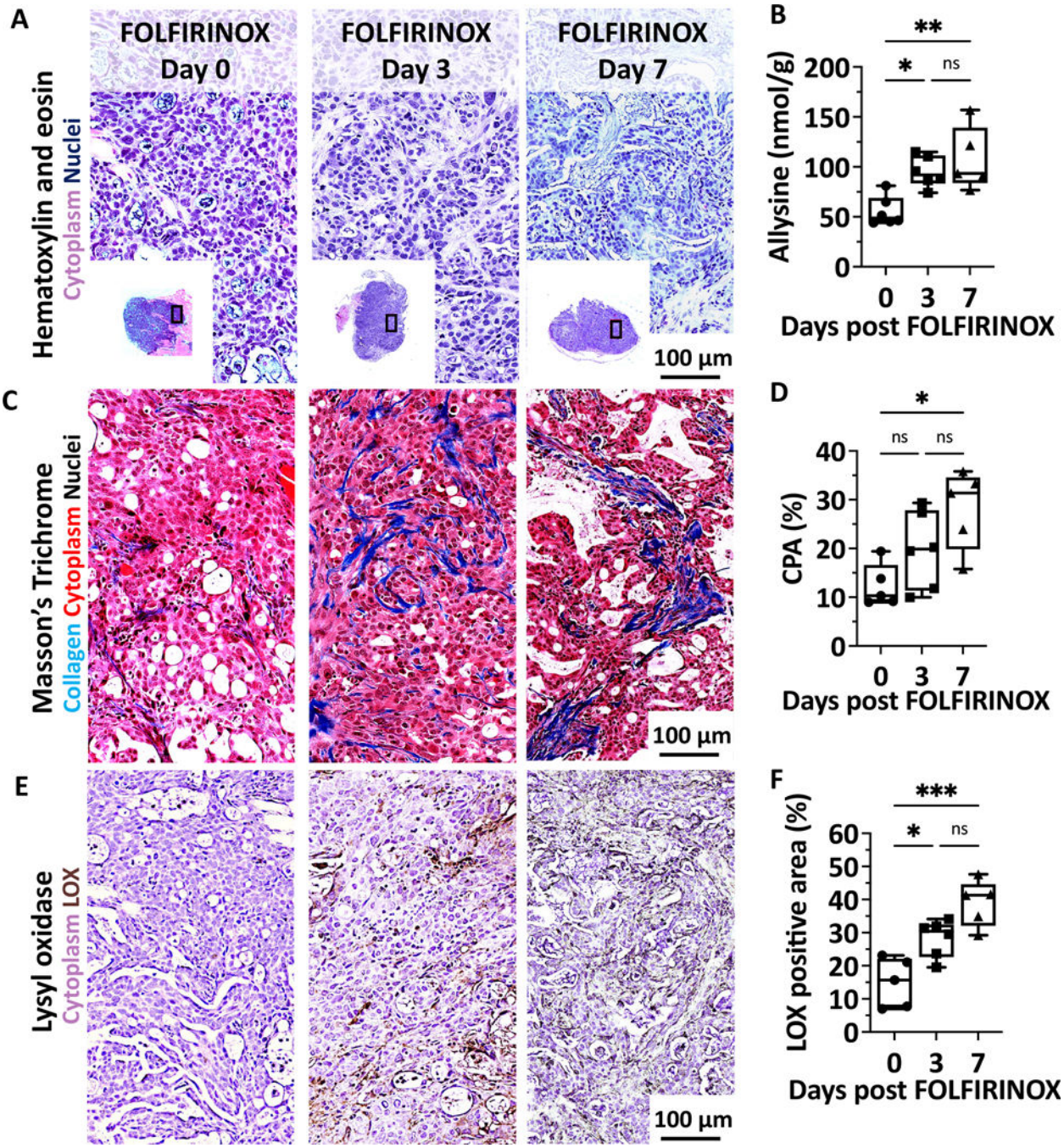

Figure 2.

Histological and biochemical characterization of PDAC6 tumor before and after FOLFIRINOX treatment. Representative hematoxylin and eosin (H&E, **A**), Masson's Trichrome (MT, **C**), and lysyl oxidase (LOX, **E**) staining of the tumor before and after one or two doses of FOLFIRINOX treatment (Scale bar, 100 µm). (**B**) Compared to the untreated tumor, allysine content was significantly increased, 1.7-fold, after one dose of FOLFIRINOX treatment and remained significantly elevated after two doses of treatment (n = 6 for Day 0 and Day 3, n = 5 for Day 7). (**D**) Collagen proportional

area (CPA) measured from MT-stained tumor sections showed that collagen deposition was only significantly elevated after two doses of treatment. (**F**) The percentage of LOX-positive tissue measured from IHC LOX-stained tumor sections showed that LOX enzyme expression was significantly elevated (1.9-fold) after one dose of FOLFIRINOX treatment and remained significantly elevated after two doses of FOLFIRINOX treatment. (n = 5 for Day 0, n = 6 for Day 3, and n = 5 for Day 7). One-way ANOVA with Tukey's post hoc test, *P<0.05, **P < 0.01, ***P < 0.001, ns, not significant).

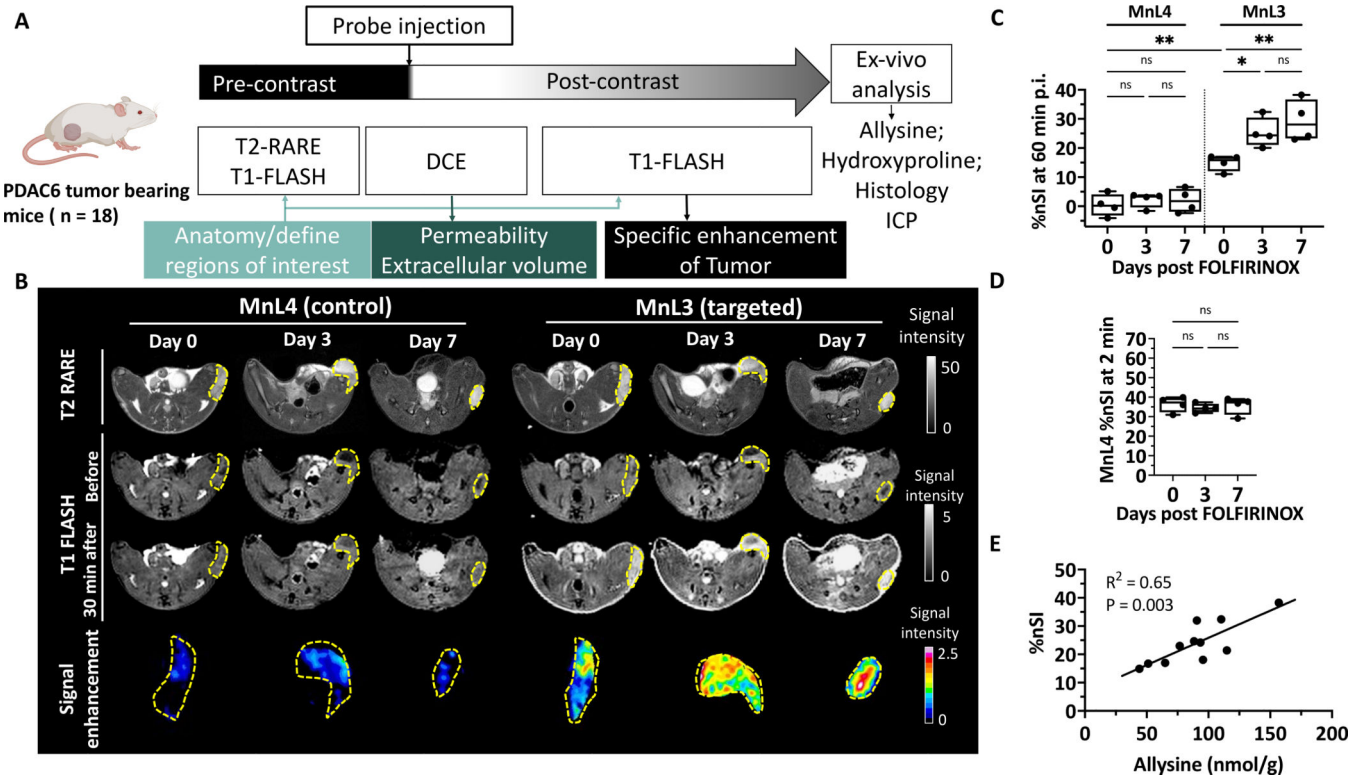

Figure 3.

Allysine-targeted molecular MR imaging of a PDAC6 mouse model of human PDAC before and after FOLFIRINOX treatment. (**A**) The diagram shows the imaging protocol (Created with BioRender.com). Anatomical 2D T2w RARE and 3D T1w FLASH MR images were acquired before probe injection to define regions of interest (ROIs). Pre- and post-injection (p.i.) 3D T1w FLASH images were acquired dynamically until 60 min after administration of the probe and used to quantify the signal within the tumor before and after probe injection. 2D T1w DCE images were acquired 1 min pre-injection and dynamically for 6 min p.i. with 5 second intervals to measure initial tumor signal enhancement. (**B**) Representative T2w images before injection of the probe, T1w images of PDAC6 tumor-bearing mice before and 30 min p.i. of MnL3 or MnL4 (0.1 mmol/kg, i.v.), and tumor MRI enhancement profile generated by subtraction of the 3D T1w images acquired before and 30 min after injection of the probes. PDAC6 tumor-bearing mice were imaged before (Day 0) and after one dose (Day 3) or two doses (Day 7) of FOLFIRINOX therapy; animals were imaged first with MnL4 followed by MnL3 4 h later. (**C**) Tumor percentage change of normalized signal intensity (%nSI, normalized to an adjacent phantom) at 60 min p.i. of probe (n = 4 for each group). (**D**) Tumor peak %nSI in 2D T1w DCE images after injection of MnL4 was unchanged before and after FOLFIRINOX treatment (n= 4 for each group). (**E**) The tumor %nSI produced by MnL3 (60 min p.i.) correlates well with allysine content. One-way ANOVA with Tukey's post hoc test, *P<0.05, **P < 0.01, ns, not significant.

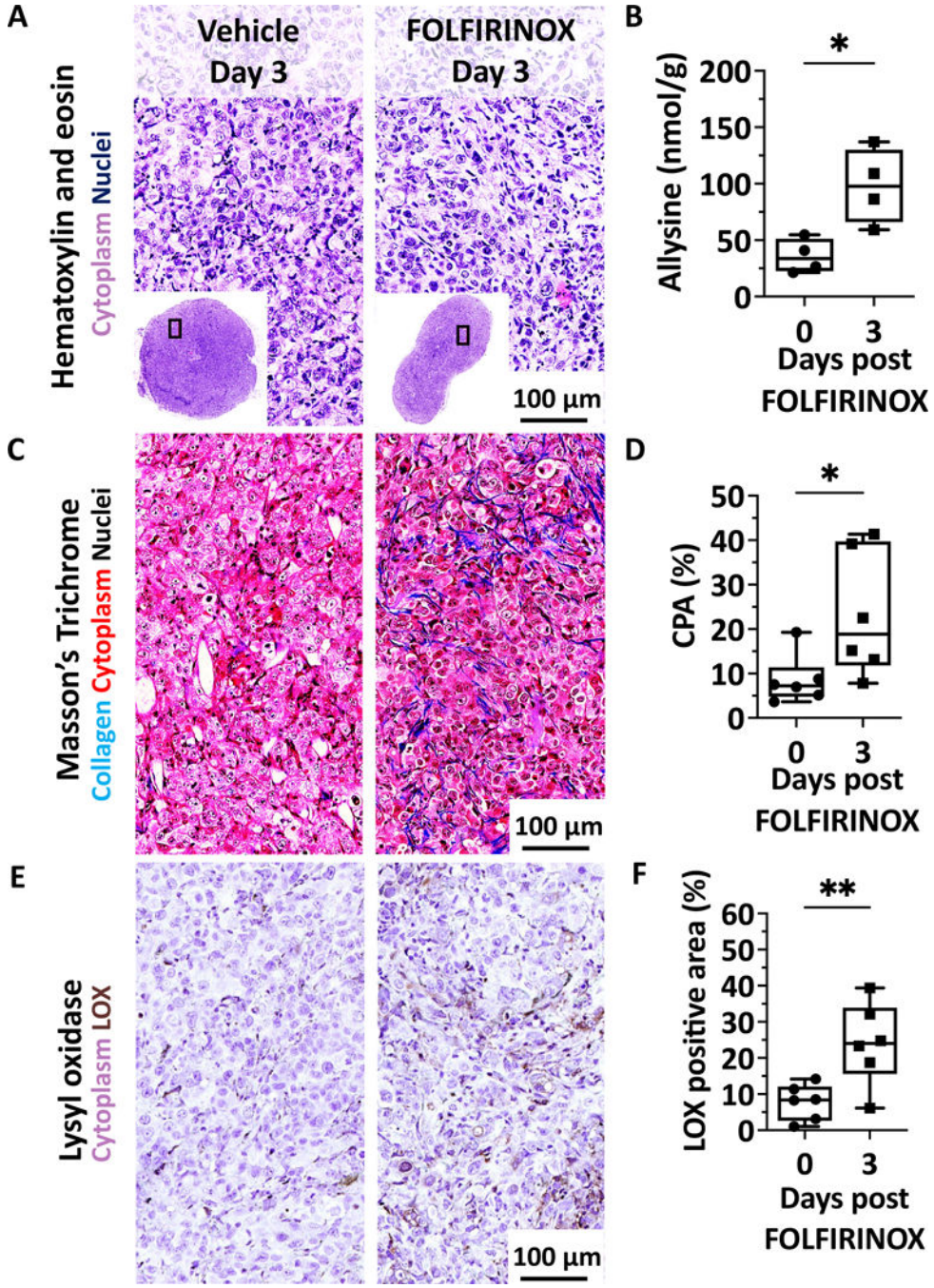

Figure 4.

Histological and biochemical characterization of PANC1 tumor before and after FOLFIRINOX treatment. Representative hematoxylin and eosin (H&E, **A**), Masson's Trichrome (MT, **C**), and lysyl oxidase (LOX, **E**) staining of the PANC1 tumor before and after one dose of FOLFIRINOX treatment (Scale bar, 100 µm). (**B**) Compared to the vehicle-treated mice, tumor allysine content was significantly increased, 2.7-fold, after one dose of FOLFIRINOX treatment (n = 4 for each group). The collagen proportional area (CPA) measured from MT-stained tumor sections (**D**) and the percentage of LOX-positive

tissue measured from IHC LOX-stained tumor sections (**F**) showed significantly elevated collagen deposition (2.7-fold) and LOX enzyme (3.1-fold) after one dose of FOLFIRINOX treatment compared to vehicle (n = 6 for each group). Student's t-test, two-tailed, *P<0.05, **P < 0.01.

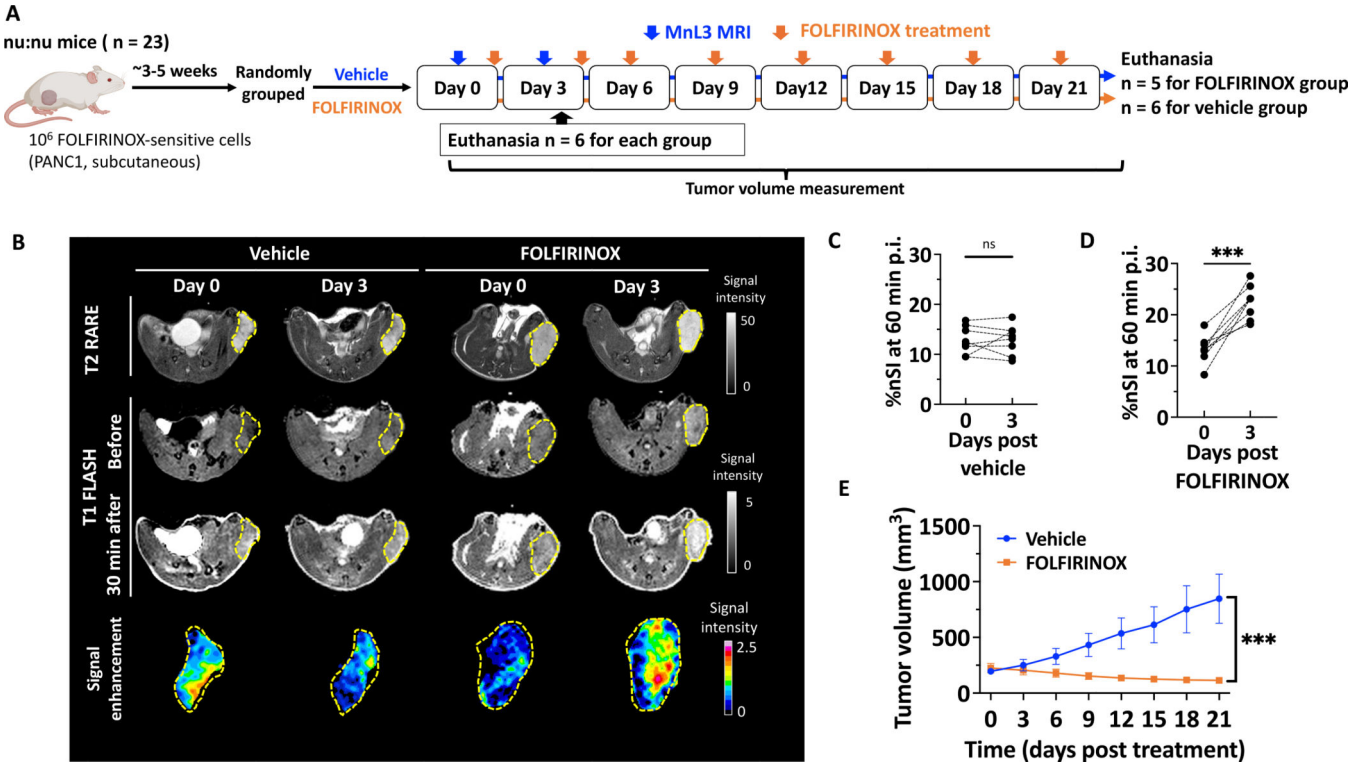

Figure 5.

MnL3 molecular MR predicts effective chemotherapy as early as 3 days after initiating treatment. (**A**) Diagram shows experimental design, animal group classification, in vivo MRI imaging, and ex vivo validation of PANC1 tumor-bearing nude mice. Blue arrows indicate time points when the MRI was performed, and orange arrows indicate when FOLFIRINOX or vehicle treatment was given (Created with BioRender.com). (**B**) Representative 2D T2w RARE images before MnL3 injection, 3D T1w FLASH images before and 30 min post-injection (p.i.) of MnL3 (0.1 mmol/kg, i.v.), and tumor MRI enhancement profile generated by subtraction of the pre-injection T1w image from the 30 min p.i. image. Mice were imaged before (Day 0) and after one dose (Day 3) of FOLFIRINOX or vehicle. Pair-wise comparison of %nSI at 60 min p.i. of MnL3 before and after one dose of vehicle (**C**) or FOLFIRINOX (**D**) (n = 8 for each group. Paired t-test, two-tailed. ***P < 0.001, ns, not significant). (**E**) Tumor volume after repeated administration of vehicle or FOLFIRINOX over 21 days. (n = 5 for FOLFIRINOX-treated group and n = 6 for vehicle-treated group. Repeated two-way ANOVA. ***P < 0.001. Mean ± SEM).

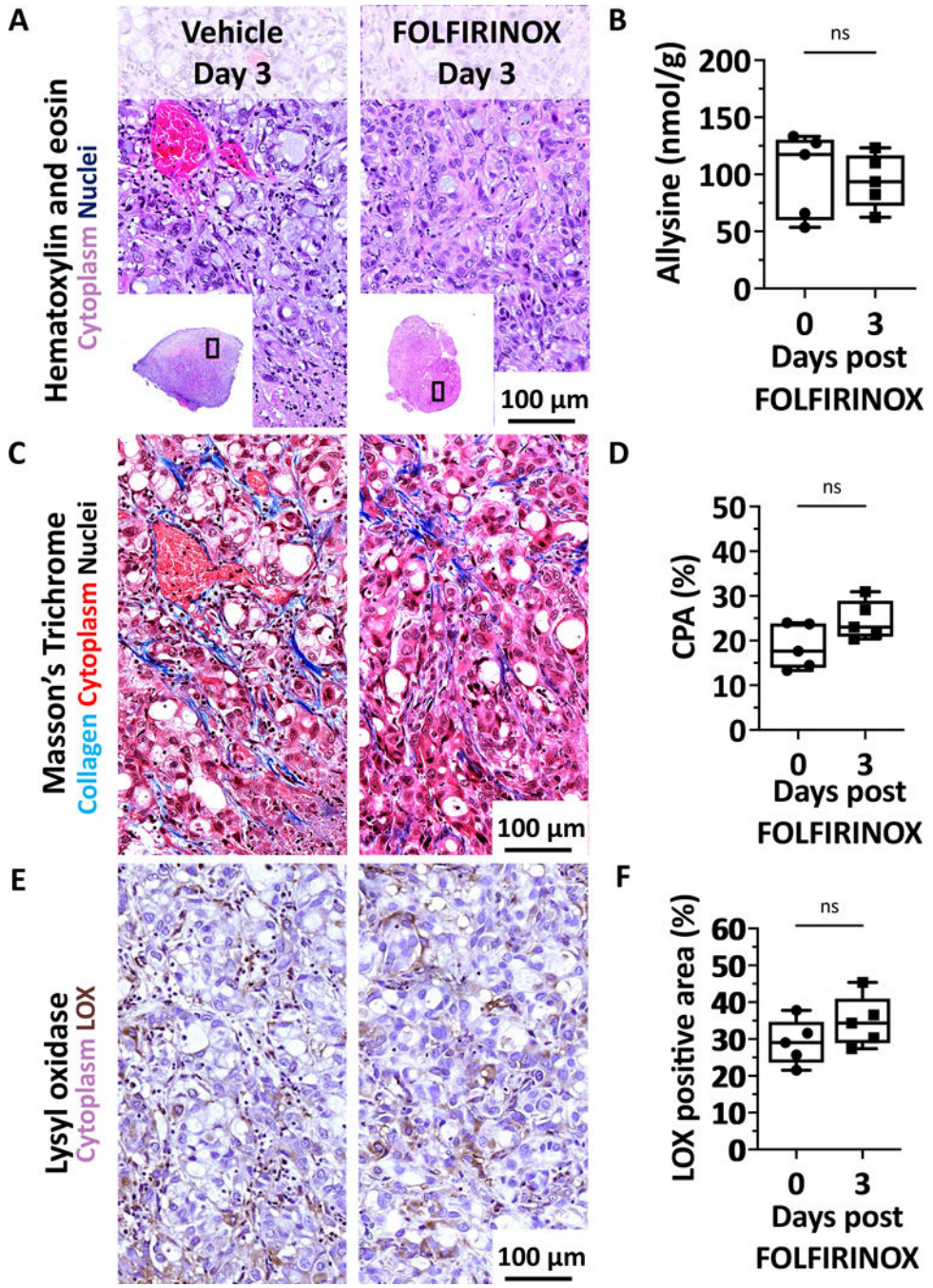

Figure 6.

Histological and biochemical characterization of 1319 tumor before and after FOLFIRINOX treatment. Representative hematoxylin and eosin (H&E, **A**), Masson's Trichrome (MT, **C**), and lysyl oxidase (LOX, **E**) staining of the 1319 tumor before and after one dose of FOLFIRINOX treatment (Scale bar, 100 µm). (**B**) Allysine tumor content was similar after one dose of FOLFIRINOX treatment or vehicle (n = 5 for each group). CPA measured from MT-stained tumor sections (**D**) and the percentage of LOX-positive tissue measured from LOX IHC stained tumor sections (**F**) showed no significant change in collagen deposition

and LOX enzyme expression after one dose of treatment compared to vehicle (n = 5 for each group). Student’s t-test, two-tailed, ns, not significant.

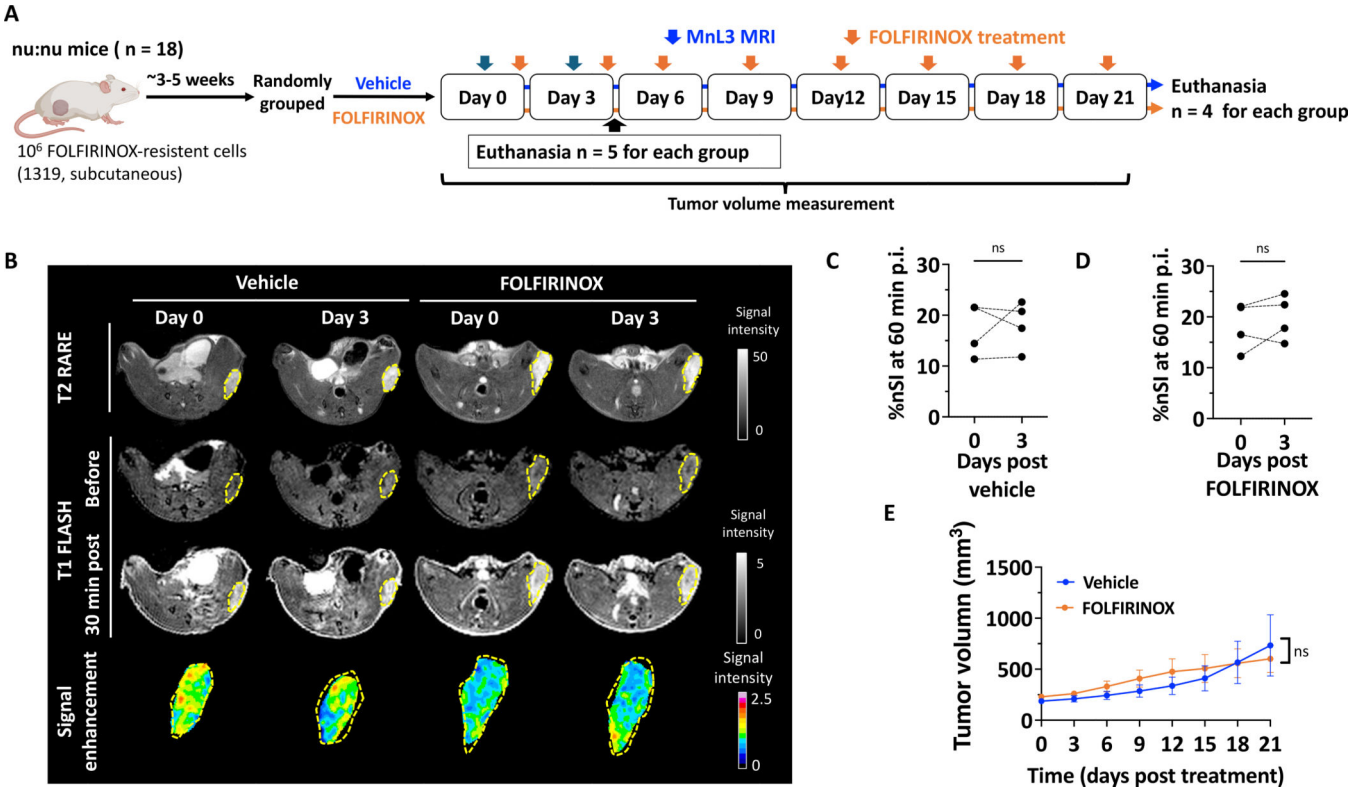

Figure 7. MnL3 molecular MR predicts ineffective chemotherapy as early as 3 days after initiating treatment.

(**A**) Diagram shows experimental design, animal group classification, in vivo MRI imaging, and ex vivo validation of 1319 tumor-bearing mice. Blue arrows indicate time points when the MRI was performed, and orange arrows indicate when FOLFIRINOX or vehicle treatment was given (Created with BioRender.com). (**B**) Representative 2D T2w RARE images, 3D T1w FLASH images before and 30 min p.i. of MnL3 (0.1 mmol/kg, i.v.), and tumor MRI enhancement profile generated by subtraction of the pre-injection T1w image from the 30 min p.i. image. Mice were imaged before (Day 0) and 3 days after the first dose (Day 3) of FOLFIRINOX or vehicle. Pair-wise comparison of %nSI at 60 min p.i of MnL3 before and after one dose of vehicle (**C**) or FOLFIRINOX (**D**) showed no significant difference in signal enhancement (n = 4 for each group. Paired Student's t-test, two-tailed. ns, not significant). (**E**) Tumor volume after repeated administration of vehicle or FOLFIRINOX over 21 days showed progression in both groups. (n = 4 for each group. Repeated two-way ANOVA, ns, not significant. Mean ± SEM).